The International Journal of Advanced Manufacturing Technology (2018) 95:2357–2368
https://doi.org/10.1007/s00170-017-1392-9

ORIGINAL ARTICLE

Understanding and overcoming of abnormity at start and end of the weld bead in additive manufacturing with GMAW

Zeqi Hu [1,2,3] · Xunpeng Qin [1,2,3] · Tan Shao [1,2] · Huaming Liu [1,2]

Received: 16 July 2017 / Accepted: 13 November 2017 / Published online: 22 November 2017

Abstract
Weld bead geometry at start and end of the bead is often abnormal compared with the middle region, which will greatly affect the forming in gas metal arc welding (GMAW) additive manufacturing. The study's aim is to investigate the causes and the optimization strategy of the weld bead abnormity at the unstable region. The weld pool dynamics, convection, and the extension process were analyzed through a three-dimensional transient fluid model and the finite element analysis of thermal behavior. The results showed that the abnormal bead geometry can be attributed to the backward fluid flow and the metal swelling in the weld pool, and the length of the initial bulky region is positively correlated with the inclined shape at the end, as well as the length of the weld pool. Some strategies to control the bead abnormity through adjusting the welding parameters, the crater filling options, and the path planning patterns were proposed. These methods contributed to the continuous and smooth deposition surface and laid the foundation of GMAW-based additive manufacturing process.

Keywords GMAW · Additive manufacturing · Start and end of the bead · Abnormity · Geometry optimization

1 Introduction

Additive manufacturing (AM) is increasingly prevalent worldwide in recent decades [1, 2]. The three-dimensional (3D) objects were fabricated by adding layer-upon-layer of material, which is extremely different from the traditional subtractive manufacturing and results in a higher material utilization and production efficiency. Components of almost any complex shape can be produced through the AM technology [3]. Gas metal arc welding (GMAW) is widely used in joining materials and repairing. Due to high deposition efficiency, low cost, automatic operation, and excellent mechanical property, GMAW is also applied in the additive manufacturing for large components. The desired properties in the GMAW-based AM are good geometrical accuracy, high strength, and low residual stress and distortion [4]. Zhou et al. [5] proposed a novel adaptive slicing algorithm which demonstrated an acceptable efficiency and high accuracy. Ding et al. [6] presented an algorithm to automatically generate optimal toolpaths for the wire and arc additive manufacturing (WAAM) process for a large class of geometries. Numerous researchers investigated the relationship between welding parameters and the weld bead geometry [7], and the width, height, penetration, and dilution rate were predicted and optimized through the regression algorithm or neural network [8], etc. The weld pool dynamics [9] and thermo-mechanical behavior [10] in multi-layer and multi-pass weld overlaying were analyzed via the finite element method (FEM), to achieve the proper heat input and low distortion.

Weld bead geometry at start and end of the bead is often abnormal compared with the middle region. In Fig. 1a, the profile is high and wide at the bead start where the arc strikes, while low and slant at the end of the bead where the arc stops [11]. This is an ordinary phenomenon and does not matter in the traditional application of joining materials. However, for multi-layer and multi-pass GMAW-based fabrication, the abnormity of the weld bead would accumulate and deteriorate with the increasing of the deposit layers, as is shown in Fig. 1b. It would affect the stability of the added-layer manufacturing, drastically

✉ Xunpeng Qin
qxp915@hotmail.com

[1] School of Automotive Engineering, Wuhan University of Technology, Wuhan 430070, China

[2] Hubei Key Laboratory of Advanced Technology for Automotive Components, Wuhan 430070, China

[3] Hubei Collaborative Innovation Center for Automotive Components Technology, Wuhan 430070, China

Fig. 1 **a** Single weld bead. **b** Thin-walled part with 16 layers single-pass deposited in the same direction (zig)

reduces the geometrical accuracy, and the significant deviation from the start to the end of the bead even terminates the subsequent deposition [3]. Therefore, the bead abnormity at the arc striking and stopping region could not be ignored and needs to be investigated and optimized. Kim et al. [12] proposed a passive vision-sensing system for real-time detection and control of the bead height and width, but it was only suitable in the middle region of the bead, rather than the arc start and end point. Hybrid layer manufacturing processes have been developed recently, which employed intermediate machining of the upper surface between successive layer depositions to avoid the cumulative deviations in the building direction [13]. However, such cleaning steps increased the complexity of the procedure and reduce the productivity [6]. Zhang et al. [3, 11] adjusted the crater filling options and the deposition parameters at the start and end segments of the weld to control the bead geometry. Ding et al. [6] applied a continuous toolpath generation strategy to avoid the frequent starting-stopping sequences.

Although these methods could overcome the uneven surface and improve the accuracy to some extent, the geometry optimization in arc striking and stopping region is incomplete. The forming fundamental mechanism of the abnormal appearance at both ends of the bead is not entirely comprehended, and the effective optimization methods are required. Therefore, in this paper, to understand the forming characteristics at the arc striking and stopping at both ends of the weld bead, a three-dimensional transient computational fluid dynamics (CFD) model was developed to simulate the molten metal flowing and solidifying in the weld pool. The bead forming in the arc striking and stopping region was investigated considering the arc pressure, the droplet impingement, and the temperature distribution. The relationships between the length of the unstable region and the weld pool were analyzed through the welding thermal FEM simulation, and the influence of the welding parameters on the bead abnormity was discussed. Then, several different control strategies were proposed according to some typical components, which were validated through the deposition experiments.

2 Experimental procedures

Experiment was conducted on a special welding equipment consisting of a five-axis work platform, a numerical control system, a welding power supply, and the other auxiliary setup. As is revealed in Fig. 2, the welding torch was clamped on the spindle with a customized fixture and the welding torch angle can be adjusted. Because of the five-axis configuration and the adjustable welding angle, the altering welding parameters and the fabrication of complex components were realizable. The direct-current power supply HUGONG NB-500S was applied to the GMAW process.

Deposition was implemented on a mild steel substrate ($150 \times 100 \times 10$ mm^3). The AWS ER70S-6 copper-coated solid wire of diameter 1.2 mm was selected as the filler material with a composition C (0.06~0.15%), Mn (1.40~1.85%), Si (0.8~1.15%), Ni (≤ 0.15%), and Cr (≤ 0.15), which melted, detached, and impinged onto the substrate in the form of droplets. The shielding gas was a mixture of 95% Ar and 5% CO_2 with a flow rate of 15 L/min. During the welding process, the communication between the platform and the power supply was established by an electromagnetic relay that receives the command signal from the numerical control system, switching the arc striking and stopping operation through the NC code. The torch travels along X, Y, and Z axes or rotates around X and Z axes at a certain speed in relation to the platform; thus, the weld bead in line, circle, or any arbitrary curve can be deposited.

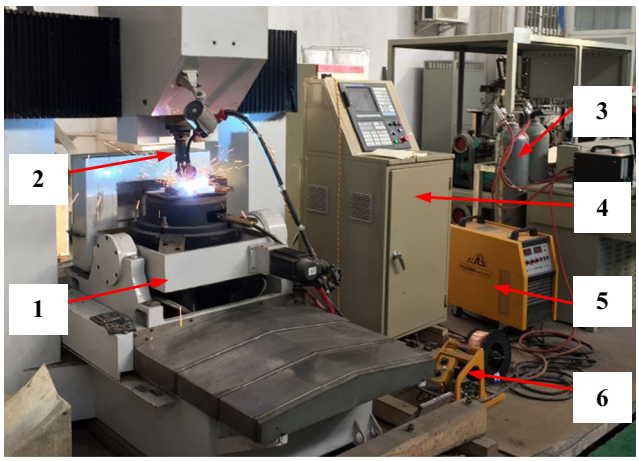

Fig. 2 Five-axis automatic surfacing welding equipment. (1) Five-axis work flat, (2) welding torch, (3) shielding gas, (4) NC cabinet, (5) welding power supply, and (6) wire feeder

There are several main variables in GMAW that affect both the penetration into the base material and weld bead profile above the base material: welding current, arc voltage, torch angle, contact tip to work distance (CTWD), and the torch travel speed. In general, welding current is directly related to wire feed speed. Namely, the welding current changes simultaneously as the wire feed speed varies and vice versa. The welding current varied from 100 to 380 amperes (A), and the arc voltage ranged from 15 to 40 volts (V). Different welding parameters lead to different weld geometry and properties, even result in the weld defect or forming failure, such as incomplete fusion, over flowing, hump, and scallop [14]. The welding current and the travel speed account for more remarkable impact on the weld bead profile over the other variables as is shown in Fig. 3, and Fig. 4 depicted the correlations between the welding parameters and the bead appearances built after repeated preliminary experiments. In this paper, the focus lies on the understanding of the abnormity at start and end of the bead and the appearance optimization, rather than the welding defect mentioned above. Therefore, the main variables should be constrained in the scope B, where the weld bead with normal appearance could be deposited.

To observe the bulky appearance at the bead start and the inclined shape at the bead end, eight beads (100 mm) were deposited with different groups of parameters in Table 1. In groups 1 to 4, the torch travel speed was set at 500 mm/min and the welding current and voltage incrementally increased. In groups 5 to 8, the travel speed increased, while the current and voltage remained unchanged. The torch was maintained perpendicular to the substrate, and the CTWD was 16 mm, and the weld beads are shown in Fig. 5. The height of the weld bead longitudinal cross-section and the length of the abnormal region were measured through the vernier caliper.

3 Modeling and numerical investigation of the weld pool dynamics

GMAW is a complicated process that involves the interactive coupling between the arc plasma, arc heat input, melting of the electrode, droplet deformation, detachment, and the periodical

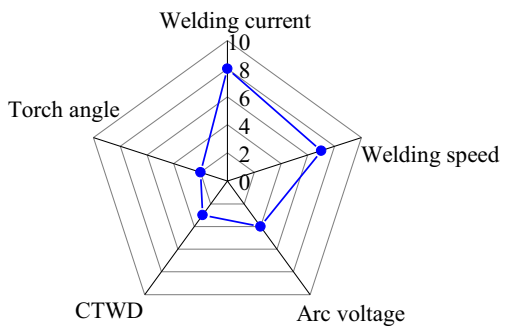

Fig. 3 The influence of welding parameters on the weld bead geometry

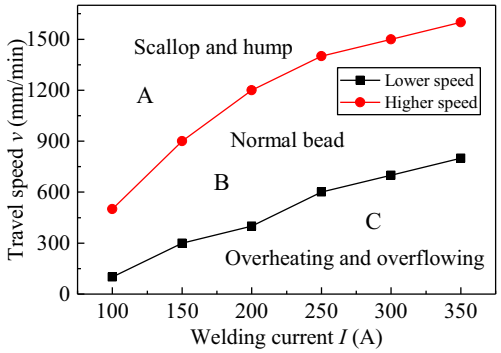

Fig. 4 Correlations between main parameters and weld bead geometry

impingement onto the workpiece [15]. During welding process, the weld pool is under the comprehensive effect of the droplet impingement, gravity, electromagnetic force, plasma arc force, and surface tension force (Marangoni effect), as shown in Fig. 6.

To simulate the weld pool and analyze the fluid flow and heat transfer in GMAW, three-dimensional transient computational fluid dynamics (CFD) models were developed, and the process was assumed as continuous droplets impinging onto the substrate with high temperature and speed, considering the arc heat input and the arc forces. Goldak's double-ellipsoidal volume heat source model [16] was applied, which is mostly used in the GMAW welding simulation, approximating the heat flux on the weld pool with a three-dimensional double-ellipsoidal configuration. It is described by the following equations:

$$\begin{aligned} q_f(x,y,z) &= \frac{6\sqrt{3}f_f Q}{a_f bc\pi\sqrt{\pi}}\exp\left(-\frac{3x^2}{a_f^2}-\frac{3y^2}{b^2}-\frac{3z^2}{c^2}\right), x\geq 0 \\ q_r(x,y,z) &= \frac{6\sqrt{3}f_r Q}{a_r bc\pi\sqrt{\pi}}\exp\left(-\frac{3x^2}{a_r^2}-\frac{3y^2}{b^2}-\frac{3z^2}{c^2}\right), x < 0 \\ f_f + f_r &= 2, \qquad Q = \eta UI \end{aligned} \tag{1}$$

where q_r and q_f are the heat flux on the front and the rear semi-ellipsoid, respectively; η is the arc efficiency; U is the arc

Table 1 Welding parameters in the experiment

Weld ID number	Current, I (A)	Voltage, U (V)	Travel speed, TS (mm/min)
1	200	20.7	500
2	250	23.2	500
3	300	25	500
4	350	27.8	500
5	300	25	300
6	300	25	700
7	300	25	1100
8	300	25	1500

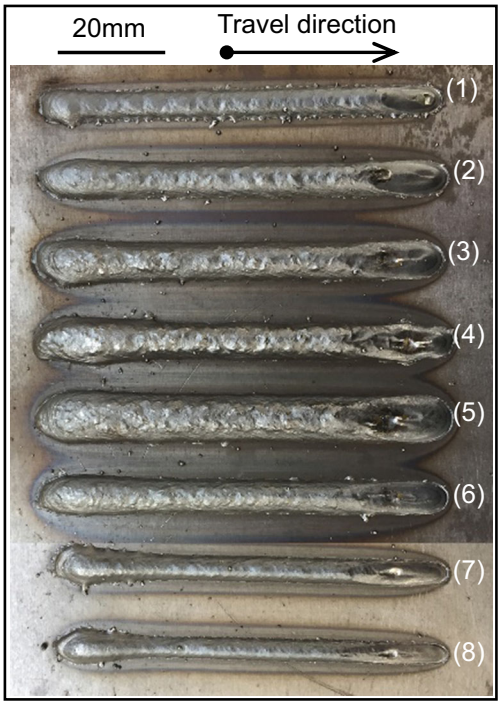

Fig. 5 Weld beads with parameters in groups 1 to 8 of Table 1

voltage; I is the welding current; a_f is the front ellipsoidal semi-axis length; a_r is the rear ellipsoidal semi-axis length; b is the half width; c is the depth; and f_f and f_r are the fraction of heat deposited in the front and the rear regions, respectively.

The body force contains the electromagnetic and buoyancy forces, which can be calculated by the following equation:

$$F_b = \vec{J} \times \vec{B} - \rho\beta g(T - T_m) \tag{2}$$

where the electromagnetic force is calculated based on Tsao's analytical solution [17]. $\vec{J}$ is the welding current density, $\vec{B}$ is the magnetic induction, ρ is the density of the workpiece, β is the coefficient of the thermal expansion, g is the acceleration of the gravity, T is the temperature, and T_m is the melting point of the workpiece.

The arc pressure acting on the free surface of the weld pool is determined by the Gaussian density distribution [18]:

$$P_{\text{arc}}(x,y) = \frac{\mu_0 I^2}{4\pi\sigma_j^2}\exp\left(\frac{r^2}{2\sigma_j^2}\right)$$
$$r = \sqrt{(x-x_0)^2 + (y-y_0)^2} \tag{3}$$

where r is the distance from the arc column center, μ_0 is the magnetic permeability of vacuum, and σ_j is the arc pressure distribution coefficient. It should be pointed out that the arc force in Eq. (3) is adopted from the GTAW welding process due to the lack of an arc force expression for GMAW at present.

The droplet is assumed to be spherical with a radius of r_d, which only has an initial vertical ($-Z$ axis) velocity of −0.5 m/s, and the temperature is set to be 2600 K. The frequency can be calculated through the following equation based on the mass conservation of the wire feed and the droplets:

$$f_d = \frac{3v_w d_w^2}{16 r_d^3} \tag{4}$$

where d_w is the diameter of the filler wire and v_w is the wire feed speed at a certain welding current.

The thermal properties such as thermal conductivity and special heat capacity are defined according to the previous study [9].

The commercial software FLOW3D was applied to solve the governing equations of energy, momentum, and mass continuity, and the relevant physic model, such as heat transfer, steel solidification process, liquid evaporation, buoyancy force, and surface tension force. The volume of fluid (VOF) method is used to trace the transient free surface of the weld pool. Only half of the workpiece ($300 \times 8 \times 16$ mm^3) was taken as the computational domain for the symmetrical structure. Figure 7 shows the meshing of the computational domain

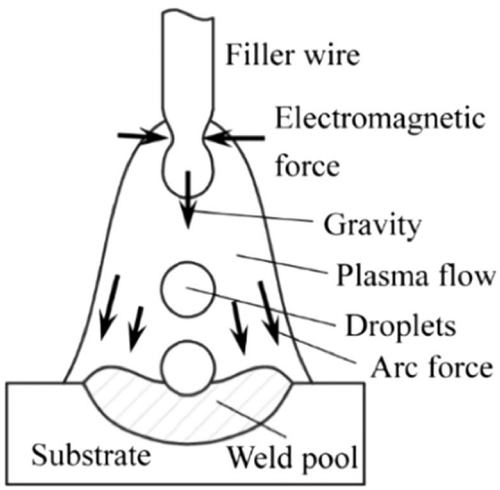

Fig. 6 Schematic representation of the driving forces in GMAW process

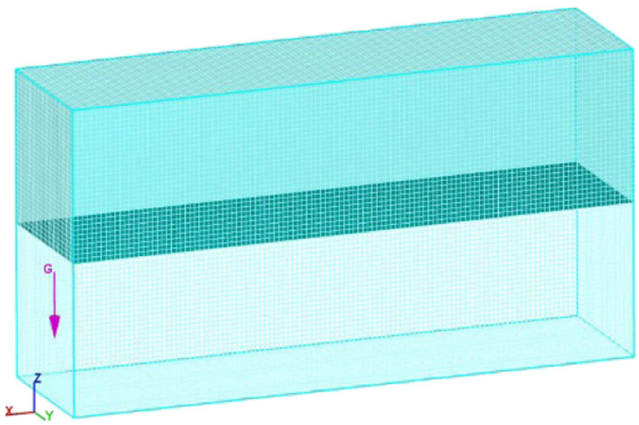

Fig. 7 The meshing of computational domain

with the cell size of 0.25 mm, which is enough to describe the free surface of the weld pool fluid flow. The calculation of coupled temperature and velocity fields are performed by the pressure-implicit with splitting Lagrangian method, and the initial time step is 2.5×10^{-5} s.

4 Results and discussion

4.1 Understanding of the weld pool convection

The GMAW has two heat source inputs, the droplet transfer and the arc heat inputs, which contribute to the fusion of the substrate and the forming of the weld pool, as shown in Fig. 8. The red area represents the molten metal where the temperature exceeds the melting point (1790 K). The liquid inside the pool is flowing, and the arrows represent the flow direction and velocity. For the interaction of periodically impingement of droplets and the arc pressure, the weld pool under the arc column was stirred and depressed, resulting in a weld crater. Simultaneously, with the torch moving along the welding direction at a certain speed, the fluid flow was thrown to the tail

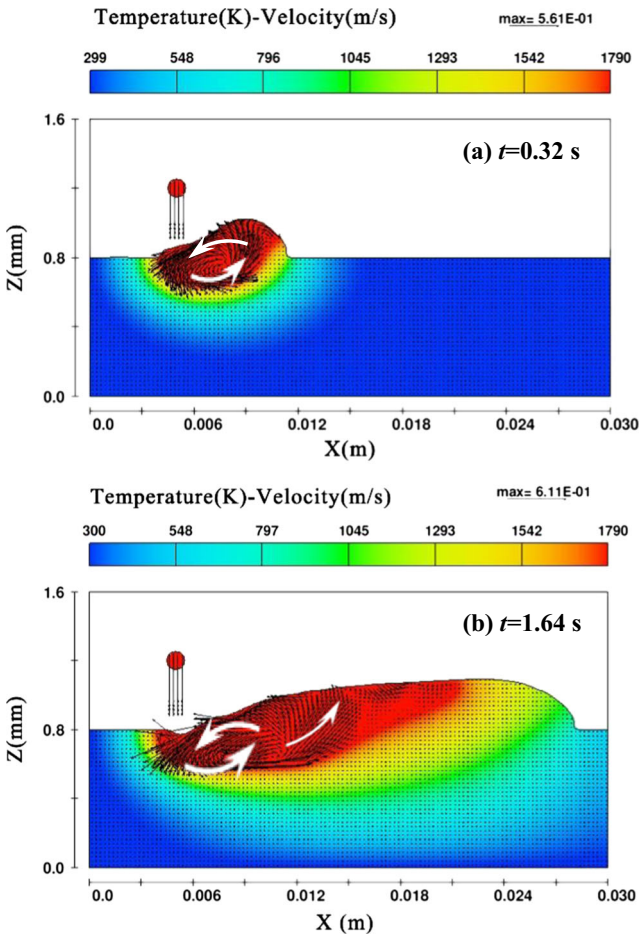

Fig. 8 Temperature (K) and velocity field of weld pool fluid flow in longitudinal cross-section ($y = 0$). **a** $t = 0.32$ s. **b** $t = 1.64$ s

of the weld pool for the liquid wetting effect, which yields an inclined shape behind the arc column, and the fluid flow at the tail has the tendency to reflux back due to the influence of the gravity, as is illustrated in Fig. 8b.

After the arc striking, the welding process presented a quasi-steady state (QSS), in which the weld pool moved with the arc column along the torch travel direction. The molten metal at the tail solidified sequentially because of the prompt heat dissipation through conduction, convection, and radiation, generating the continuous weld bead with consistent height, width, and steady profile. It can be observed that at the initial time in Fig. 8a, the weld pool is small, and there only existed the anticlockwise circulation pattern, which resulted in the accumulation and swelling of molten metal. But seconds later, an anticlockwise circulation and a backward fluid flow appeared in the long weld pool behind the arc column, so that the height of the metal accumulation was lower than that when the weld pool was small initially, which caused the bulky bead geometry at the start of the bead. As the arc stopped, the weld pool with an inclined shape has no time to perform the reflux process and solidified quickly because of the sudden interruption of heat input and the prompt heat dissipation, therefore, resulted in the slant profile at the end of the weld beads.

To validate the three-dimensional transient welding simulation, the cross-section of the actual weld bead and the simulated model are displayed, which can also be used to calibrate the simulation parameters. As is shown in Fig. 9, the width and the shape of the simulated bead coincide well with the actual bead. However, the bead height of the simulated model is lower than the actual bead by 4.45%. This is mainly because of the liquid metal loss caused by evaporation, and the droplet size and transfer frequency cannot be accurately determined. Generally, the simulation results are in good agreement with the actual experiment.

4.2 The forming characteristics of the weld bead abnormity

For all eight weld beads, the appearance at the start is bulky and larger than that at the middle part because of the material

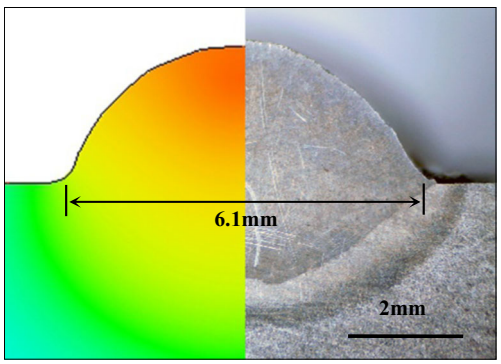

Fig. 9 Comparison of predicted and experiment weld bead geometry

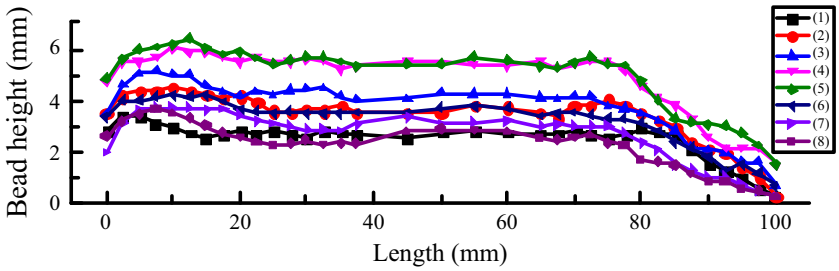

Fig. 10 Longitudinal section height of the weld beads

coagulation and decreased gradually at the end of the bead, namely the arc stopping region, where a slope profile was presented. Figure 10 shows the height in longitudinal section of the weld beads, which can illustrate the variant characteristics of the bead geometry along the length. The steady height at the middle area of the eight beads are different because of the different welding current and torch travel speed, which resulted in a different cladding rate. For the abnormal region, when the height is higher than that of the middle region by 5%, it was regarded as the initial arc striking region, while lower by 5% the bead end region. Thus, the length of the bead start and end region was measured and compared as demonstrated in Fig. 11. For beads 1 to 4, the length of the abnormal region increased with the welding current, and for beads 5 to 8, the length decreased with the torch travel speed. The Pearson product-moment correlation coefficient is calculated, where $r = 0.765$, meaning a strong positive correlation between the two variables. Besides, the inclined region approximately represented the shape of the weld pool during the GMAW [19], so it indicated that the length of the bulky region is related to the length of the inclined shape and the weld pool dimension; furthermore, they were determined by the welding parameters, such as the welding current and the torch travel speed.

As discussed above, the abnormal bead geometry at the start and end is related to the weld pool dynamics and the dimension. To analyze the correlation quantitatively, another simplified welding thermal simulation was conducted with the commercial software package SIMUFACT.WELDING, in which the filler material and arc forces were ignored for observing the weld pool profile and reducing the processing time. The welding parameters were set as the group 8 in Table 1, with the arc efficiency of 0.85. Figure 12 shows the plate ($150 \times 100 \times 10$ mm^3) and meshing quality, and the central line (100 mm) was set as the welding trajectory with the arrow denoting the torch angle.

The double-ellipsoidal heat source applied on the welding trajectory was moving along the specified direction, and the temperature of the welding area increased rapidly as is shown in Fig. 13. The red area showed shape of the weld pool where the temperature exceeded the melting point (1517 °C). As the time incrementally growing, the length of the weld pool increased significantly. Figure 14 records the position of the head, the tail, and the length of the transient weld pool. In the first 1.1 s, the head of the pool moved forward at a constant speed, while the tail of the pool moved slowly, which resulted in the gradual increase of the pool length. Subsequently, the travel speed of the tail increased to the same level with the head, and the length of the weld pool maintained invariant, namely, it reached the quasi-steady state (QSS). In this process, the metal at the head of the pool melted and at the tail, the molten metal liquid solidified synchronously, so that the pool moved along the deposition direction at a constant speed, with a steady pool length (SPL) subjected to the arc voltage, current, and torch speed and other welding parameters.

In the initial non-steady state, the weld pool experienced a process of gradual extension, during which the length of the

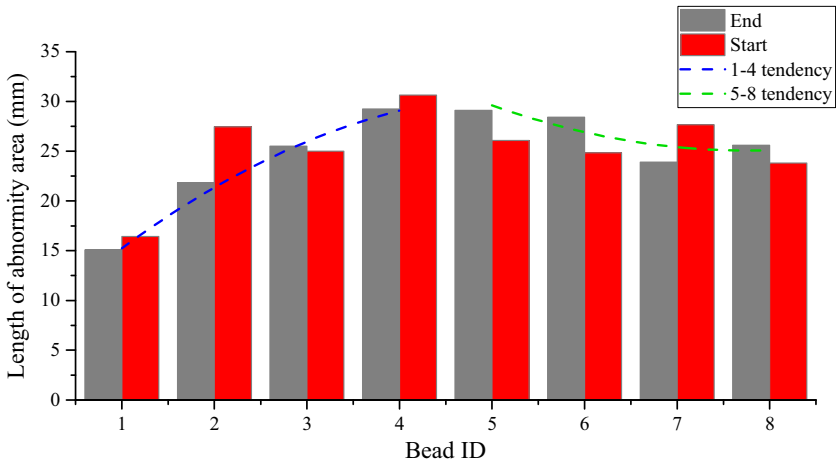

Fig. 11 The length of the abnormal region at the start and the end of the beads

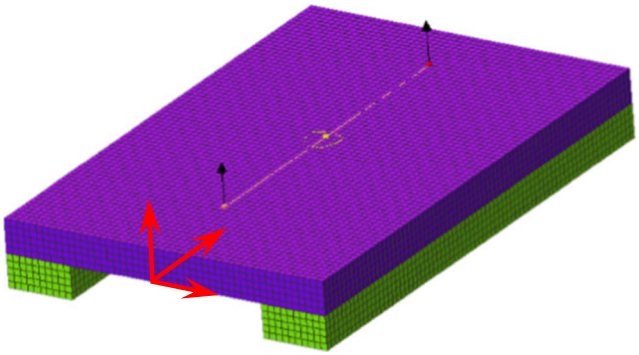

Fig. 12 The meshing condition of the welding substrate and trajectory

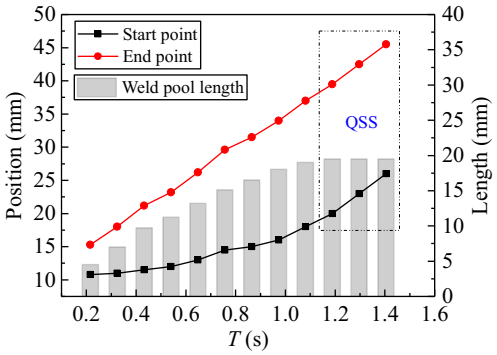

Fig. 14 Position and length of the weld pool

pool is always shorter than the QSS. As is discussed above, the molten metal in the weld pool was flowing towards the tail under the arc pressure and the droplet impingement, and the wire feed speed (WFS) was constant because of the invariant welding current and torch travel speed, so that the filler material deposited on the plate per second was equivalent. When the weld pool is small, there only exists the anticlockwise circulation of the molten metal as shown in Fig. 8a, so a higher and wider bead would be deposited with equivalent filler material. In Fig. 15, the point P_1 was the arc striking point, and when the torch was still located in the region A, the pool length was shorter than the SPL, so that the bead was bulky. Then, when the torch reached P_2, the weld pool had extended to the QSS with a steady pool length; therefore, the width and height became stable subsequently as is illustrated in region B. Furthermore, the tail of the weld pool merely moved for a relative short distance compared to the head, so that the length of the initial bulky region P_1P_2 approximated the SPL, and presented a positive correlation with the length of the inclined region at the tail of the bead.

Since the weld bead abnormity in the arc striking and stopping region is related to the dimension and dynamics of the weld pool that is subject to the main variables, welding current and the torch travel speed. Several groups of simulation were conducted with different parameters to explore the relationships with the SPL, as shown in Fig. 16. It was found that the weld pool length was inversely proportional to the torch travel speed, while proportional to the welding current, which was in agreement with the experiment. The dimension of the weld pool is determined by the heat input, and it can be explained by the following equation: $Q = \eta UI/v$. The power of the heat source increased with the current I, so that larger current would result in the larger weld pool due to more heat flux applied on the plate. In contrast, when the torch travel speed increased, the heat flux applied on the substrate of per unit length decreased; thus, a small weld pool was generated. In addition, the pool dimension in different welding heat input is demonstrated in Fig. 17, and the pool length and width revealed an increasing trend with the heat input.

5 Overcoming of the weld bead abnormity

5.1 Welding parameter adjustment

The forming characteristics of the bead abnormity are investigated above, and some measures should be taken to overcome the problem and optimize the appearance at the start and

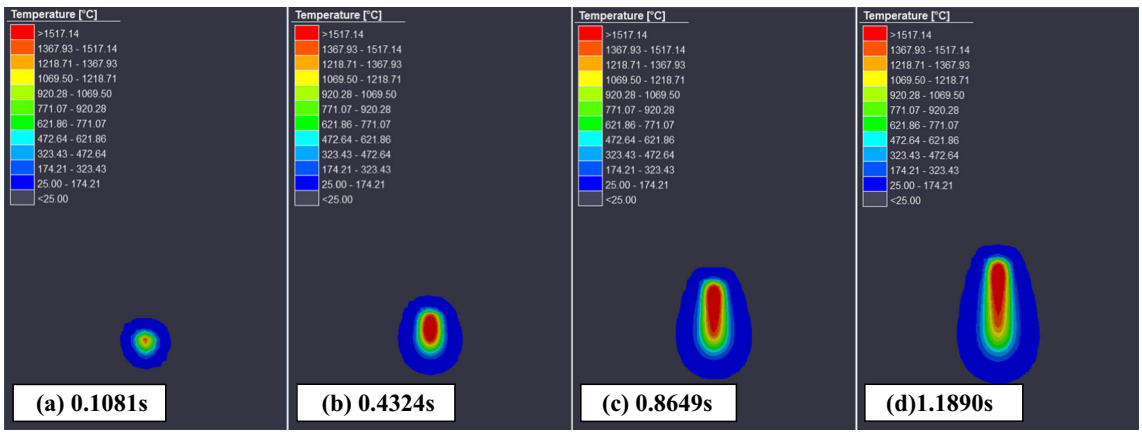

Fig. 13 Thermal field distribution in the welding simulation

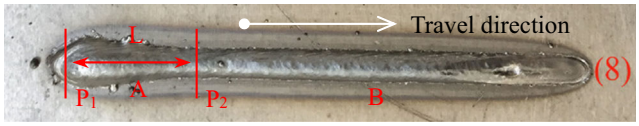

Fig. 15 The deformation at both ends of the weld bead

end of the bead. The appearance is tightly correlated with the weld pool, and it is affected by the welding parameters, such as the welding current, arc voltage, and travel speed.

The welding current not only affects the heat input, but also determines the arc force acting on the pool, which will influence the fluid flow and the inclined shape at the bead end. The arc force in GMAW was expressed with Eq. (3), which is proportional to the current squared. As the welding current increased, the depressed pool crater became deeper and wider because of the increasing arc force. On the other hand, high current will deliver massive heat flux into the pool, resulting in the delaying heat dissipation and larger pool size, so as to the severer bead abnormity. According to the welding thermal simulations and experiments in Fig. 18, the low current and high travel speed is recommended to acquire the proper weld pool and bead geometry at the start and end point.

The abnormal weld bead can also be attributed to the improper quantity of material deposition, namely, the excess material filling at the initial convex region and the inadequate material supplement at the inclined region. The quantity of the filler wire deposited onto the substrate is reversely proportional to the torch travel speed, so that the altering travel speed can be applied in the bead geometry optimization strategy. At the bead start, a higher travel speed compared to the middle part is needed to reduce the amount of filler metal to overcome the convex bead geometry, and the lower speed is utilized at the bead end to compensate for the inclined bead shape. A single bead was deposited with the welding current at 200 A and travel speed at 600 mm/min. In contrast, another single bead at the same parameters was deposited using the proposed speed control strategy. As is depicted in Fig. 19a, b, the weld pool length is approximately 15 mm; therefore, the torch speed at the initial 15 mm length is maintained at a higher speed of 800 mm/min and a lower speed of 400 mm/min at the terminal 15 mm length, respectively. The convex geometry is significantly decreased, but the depressed profile at the arc stopping area still existed because of the persistent arc force which was not affected by the decreased torch travel

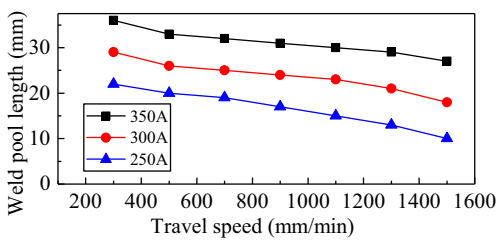

Fig. 16 Weld pool length with different deposition parameters

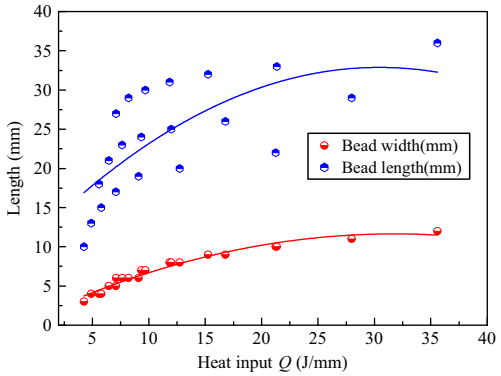

Fig. 17 The weld pool length and width with different welding heat input

speed. Besides, the power source in this experiment is provided with the crater filling option, which allows the operator presets a special welding current, arc voltage, and actuation duration to control the shape and dimension of the weld crater upon the termination of the welding process. Figure 19c shows the effect of the function with the current set at 130 A, the voltage at 17 V, and duration time of 1.5 s, and it can be seen that the crater fill feature is effective at the bead end through a lower current welding continued for a short time, so that the additional metal could be supplied into the inclined crater. Therefore, the parameter adjustment, the speed control strategy at the bead start, and the crater filling feature at the bead end could be combined together to guarantee the uniformity of the whole bead, as is shown in Fig. 19d.

5.2 Control strategy for closed path deposition

The additive manufacturing process is comprised of successive layers generated by the welding paths [20], and different path patterns will result in different surface geometries because of the weld bead abnormity at the bead start and end. The scanning path can be divided into the closed path and the open path according to whether the torch trajectory is in closed loop or open loop.

For the closed path, a cup-shaped component was deposited with the welding current set at 200 A, the voltage at 21 V, and the travel speed at 600 mm/min. The arc stroked at the start point and the welding torch rotated around the center point with the radius of 30 mm in anticlockwise direction.

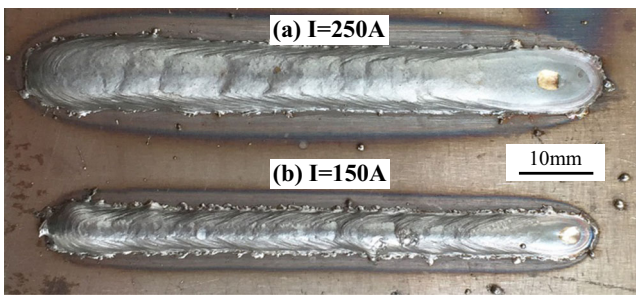

Fig. 18 Weld beads with the current at 150 and 250 A

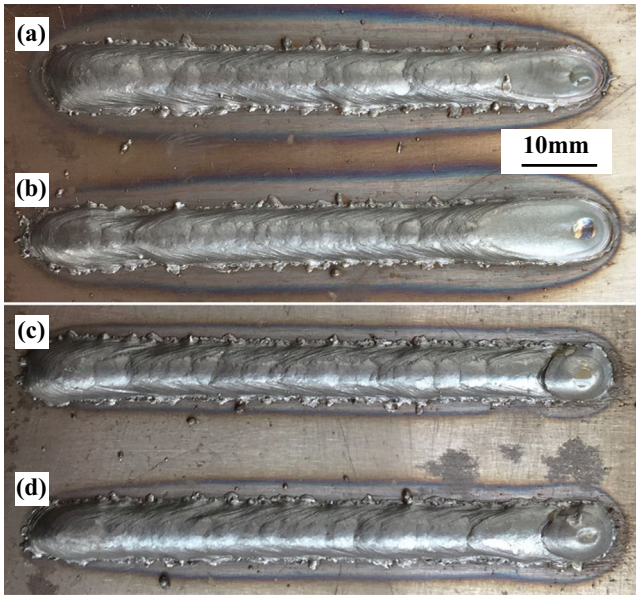

Fig. 19 Weld beads with the varied speed control strategy. **a** No control. **b** Higher speed at bead start. **c** Crater filling. **d** Higher speed at the start and crater filling at the end

After the arc stopped at the end, the torch was elevated 1.5 mm which was equal to the layer thickness and the next layer deposition proceeded. To avoid the meltdown of the previous structure due to the excessive heat input, the idle time of 20 s was applied after each layer, so that the temperature can cool down to a lower value. As is seen in Fig. 20, the height at the bead start is considerably larger than that at the end and presented an inclined shape along the circumference. Only after 13 layers the accumulated deviation at the start and end was so significant that subsequent deposition cannot be continued.

To regulate the deposited geometry, the height deviation can be counteracted through the overlapping of the bead start and end for the closed path components. Namely, the rotation angle of the torch around the center point could overstep the limitation of 360° by a certain length, so that the inclined shape at the end of the bead can be compensated by the convex geometry at the beginning. The cup-shaped part of the same dimension with 25 layers was deposited as depicted in Fig. 21, in which the overlapping length was maintained at

Fig. 21 A cup-shaped component deposited along the same direction with the overlapping strategy

8 mm in each layer. The large height deviation was successfully eliminated; nevertheless, it caused the metal knob in each layer at the overlapping position because of the excessive filling material at the junction.

Whereas the joints of weld passes can decrease the smoothness of the deposition surface, the quantity of which should be optimized to minimum so that the impact could be reduced to a low level. For the closed path components, the stager ramp strategy could be applied to guarantee the continuous spiraling welding path and avoid the arc striking and stopping in each layer with the schematic diagram shown in Fig. 22. In this pattern, the arc struck in the first layer and rotated around the center point with a radius of 40 mm until the tale of the path, then move to the upper layer along a constant ramp angle of 8° with the arc burning, so that the weld path during the whole deposition process was continuous without termination and arc stopping. Even after 20 layers were deposited, the surface of cup-shaped part was continuous and smooth without the metal knob resulted from the frequent arc interruption.

5.3 Control strategy for open path deposition

For the components with open path, the filling layer is often comprised of discrete trajectories, such as the upright wall and flat plate. The increasing of weld passes and welding joints are

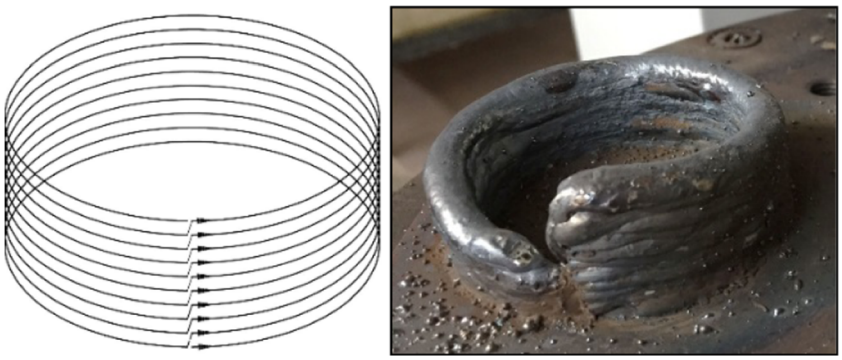

Fig. 20 A cup-shaped component deposited along the same direction without any control strategy

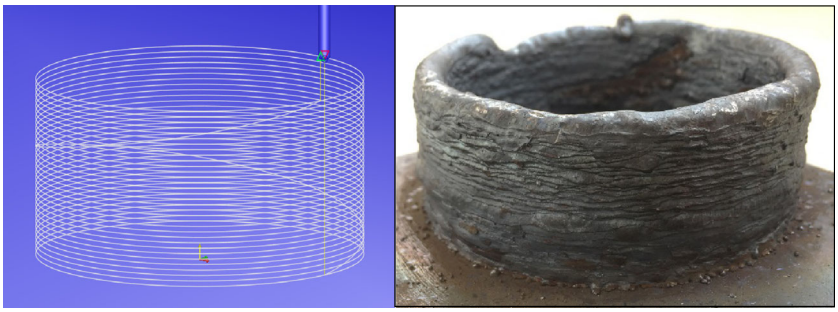

Fig. 22 Stager ramp strategy for closed path deposition

inevitable during the open path fabrication, so that the surface quality was more vulnerable due to the frequent arc striking and stopping.

A rectangular wall perpendicular to the substrate consisting of open path layers was deposited with the welding current of 200 A, the arc voltage of 21 V, the torch travel speed of 600 mm/min, and the length of the bead was 100 mm. Another flat plate of the same dimension covering the substrate was fabricated with the identical welding parameters. Two path patterns were employed to deposit the upright wall and the flat plate. One was the zig method, with which the welding direction was unidirectional, and the other was the zigzag method, with which the welding direction was alternating. As seen in Fig. 23a, only after 16 layers with zig method, the accumulated error was significant and resulted in the termination of the deposition. During the initial several layers, the bulky bead geometry at the bead start and the inclined profile at the end made it easier for the molten metal to flow downwards, leading to the gradient shape of the wall. However, this defect was avoided through the zigzag method as depicted in Fig. 23b. Since the deposition direction was alternating in every other layer, the bulky bead at the start could compensate for the inclined geometry at the end, so that the rectangular wall could be deposited successfully as devised. After deposition of 31 layers, the height was well distributed and the deviation of both ends was slight as shown in Fig. 24.

Nevertheless, the zigzag method for the flat plate was not very effective as is illustrated in Fig. 23c, d. The step-over distance was maintained at 50% of the bead width to achieve the smooth plate surface, but the lacked metal at the end of the bead could not be replenished. Therefore, the strategy of fewest joints could be applied based on the zigzag method. Namely, the arc was kept burning during the translation for the step-over when the welding direction was alternated, so that the plate can be deposited through only one continuous path, as is shown in Fig. 25. Simultaneously, the control strategy of adjusting the welding parameters could also be utilized in closed and open path deposition.

Although several optimization methods through the welding parameter adjustment and the welding path planning were proposed, some newly developed welding technology and the advanced power supply may also be useful to avoid the bead abnormity, such as the high-performance digital welding supply, the dual-pulse welding technology, and the cold metal transfer technology (CMT), which provide a more accurate control of the arc, the welding time, and the wire feed rate. Further investigation of the bead geometry optimization at the start and end of the bead could be conducted into the combination of these methods.

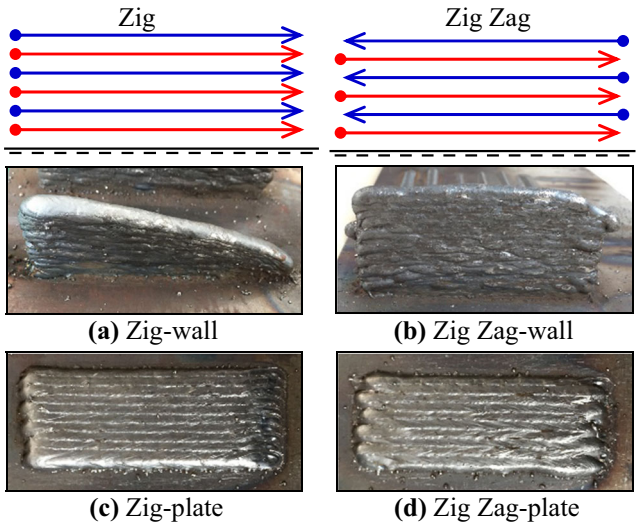

Fig. 23 The wall and plate with open path in zig and zigzag methods

6 Conclusions

In additive manufacturing with GMAW, the geometry abnormity at the start and end of the bead was

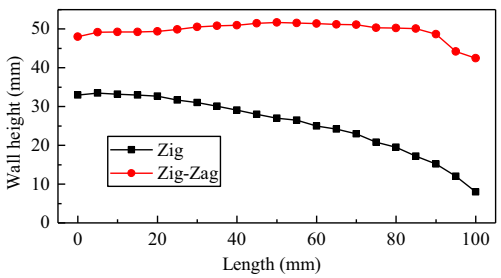

Fig. 24 The height of the upright wall

Fig. 25 Fewest joint strategy applied in the plate deposition

investigated through the transient weld pool dynamics and welding thermal field simulation, and some optimization strategies were proposed. The main conclusions could be drawn as follows:

I. The molten metal in the weld pool was depressed and presents a tendency to flow backwards. The inclined shape at the end of the bead can be attributed to the sudden shutdown of heat input and the rapid solidification stopping the fluid refluxing. After the arc striking, the weld pool experienced a process of gradual extension then reached the quasi-steady state with a constant weld pool length. Because of the shorter length in the initial non-steady state, the equivalent wire feeding volume would generate a bulkier bead geometry compared to the middle part. The weld bead profile became normal when the weld pool extended into the steady state, which accounted for the positive correlation between the length of the initial bulky region and the steady pool length, as well as that at the arc stopping region.
II. Compared with the arc voltage, torch angle, and the contact to work distance, the welding current and torch travel speed have more significant impact on the weld bead geometry at the start and the end of the bead. The small current and rapid travel speed was recommended to acquire the consistent bead profile in the whole length of the bead, and altering speed and the crater filling option was also effective.
III. For the closed path component, the overlapping pattern in which the inclined shape at the arc stopping region was compensated by the initial bulky region could result in a successful deposition. The stagger ramp pattern with the continuous weld path would generate a smooth and consistent surface. As for open path parts, the alternating direction deposition and the fewest joint strategy would produce a desirable surface quality.

Acknowledgements The authors would like to thank all the staff of Hubei Key Laboratory of Advanced Technology for Automotive Components for supporting this work.

Funding information The work was supported by the National Natural Science Foundation of China (NSFC) (No. 51575415), the Natural Science Foundation of Hubei Province under the Grant No. 2016CFA077, and the Fundamental Research Funds for the Central Universities (WUT 2017-YB-023), which are gratefully acknowledged.

References

1. Williams SW, Martina F, Addison AC, Ding J, Paradal G, Colegrove P (2016) Wire + arc additive manufacturing. Mater Sci Technol 32(7):641–647. https://doi.org/10.1179/1743284715Y.0000000073
2. Liu H, Hu Z, Qin X, Wang Y, Zhang J (2017) Parameter optimization and experimental study of the sprocket repairing using laser cladding. Int J Adv Manuf Technol 91(9-12):3967–3975. https://doi.org/10.1007/s00170-017-0066-y
3. Zhang YM, Chen Y, Li P, Male AT (2003) Weld deposition-based rapid prototyping: a preliminary study. J Mater Process Technol 135(2-3):347–357. https://doi.org/10.1016/S0924-0136(02)00867-1
4. Kannan T, Murugan N (2006) Effect of flux cored arc welding process parameters on duplex stainless steel clad quality. J Mater Process Technol 176(1-3):230–239. https://doi.org/10.1016/j.jmatprotec.2006.03.157
5. Zhou MY (2004) Adaptive slicing of functionally graded material objects for rapid prototyping. Int J Adv Manuf Technol 24(5-6):345–352. https://doi.org/10.1007/s00170-003-1623-0
6. Ding D, Pan Z, Cuiuri D, Li H (2014) A tool-path generation strategy for wire and arc additive manufacturing. Int J Adv Manuf Technol 73(1-4):173–183. https://doi.org/10.1007/s00170-014-5808-5
7. Cao Y, Zhu S, Liang X, Wang W (2011) Overlapping model of beads and curve fitting of bead section for rapid manufacturing by robotic MAG welding process. Robot Comput Integr Manuf 27(3):641–645. https://doi.org/10.1016/j.rcim.2010.11.002
8. Ghanty P, Vasudevan M, Mukherjee DP, Pal NR, Chandrasekhar N, Maduraimuthu V, Bhaduri AK, Barat P, Raj B (2008) Artificial neural network approach for estimating weld bead width and depth of penetration from infrared thermal image of weld pool. Sci Technol Weld Join 13(4):395–401. https://doi.org/10.1179/174329308x300118
9. Hu J, Guo H, Tsai HL (2008) Weld pool dynamics and the formation of ripples in 3D gas metal arc welding. Int J Heat Mass Transf 51(9-10):2537–2552. https://doi.org/10.1016/j.ijheatmasstransfer.2007.07.042
10. Zhao H, Zhang G, Yin Z, Wu L (2012) Three-dimensional finite element analysis of thermal stress in single-pass multi-layer weld-based rapid prototyping. J Mater Process Technol 212(1):276–285. https://doi.org/10.1016/j.jmatprotec.2011.09.012
11. Xiong J, Yin Z, Zhang W (2016) Forming appearance control of arc striking and extinguishing area in multi-layer single-pass GMAW-based additive manufacturing. Int J Adv Manuf Technol 87(1-4):579–586. https://doi.org/10.1007/s00170-016-8543-2
12. Kim J, Lee J (2008) A control system for uniform bead in fillet arc welding on tack welds. J Mech Sci Technol 22(8):1520–1526. https://doi.org/10.1007/s12206-008-0433-6
13. Suryakumar S, Karunakaran KP, Bernard A, Chandrasekhar U, Raghavender N, Sharma D (2011) Weld bead modeling and process optimization in hybrid layered manufacturing. CAD Comput Aided Des 43(4):331–344. https://doi.org/10.1016/j.cad.2011.01.006
14. Xiong J, Zhang G, Zhang W (2015) Forming appearance analysis in multi-layer single-pass GMAW-based additive manufacturing. Int J Adv Manuf Technol 80(9-12):1767–1776. https://doi.org/10.1007/s00170-015-7112-4
15. Wu D, Hua X, Ye D, Ma X, Li F (2017) Understanding of the weld pool convection in twin-wire GMAW process. Int J Adv Manuf

Technol 88(1-4):219–227. https://doi.org/10.1007/s00170-016-8775-1
16. Goldak J, Chakravarti A, Bibby M (1984) A new finite element model for welding heat sources. Metall Trans B 15(2):299–305. https://doi.org/10.1007/BF02667333
17. Tsao KC, Wu CS (1988) Fluid flow and heat transfer in GMA weld pools. Weld J 67:70s–75s
18. Cao Z, Yang Z, Chen XL (2004) Three-dimensional simulation of transient GMA weld pool with free surface. Weld Journal-New York- 83:169–S
19. Azar AS, Ås SK, Akselsen OM (2012) Determination of welding heat source parameters from actual bead shape. Comput Mater Sci 54:176–182. https://doi.org/10.1016/j.commatsci.2011.10.025
20. Ding D, Pan Z, Cuiuri D, Li H (2015) A practical path planning methodology for wire and arc additive manufacturing of thin-walled structures. Robot Comput Integr Manuf 34:8–19. https://doi.org/10.1016/j.rcim.2015.01.003